CrystEngComm

ROYAL SOCIETY OF CHEMISTRY

PAPER

View Article Online
View Journal | View Issue

Cite this: *CrystEngComm*, 2022, **24**, 7758

Crystal engineering of a co-crystal of antipyrine and 2-chlorobenzoic acid: relative energetic contributions based on multipolar refinement†

Aqsa Bilal,[a] Arshad Mehmood,[b] Sajida Noureen,[a] Claude Lecomte[cd] and Maqsood Ahmed *[a]

The growth and stability of a new cocrystal between antipyrine and 2-chlorobenzoic acid (**AN**–**CBA**) is analysed in terms of electrostatic and topological parameters *via* an experimental and theoretical charge density analysis. The co-crystal is thermally stable up to 140 °C. High-resolution X-ray diffraction data were collected at 100 K to carry out a multipolar refinement based on the multipolar atom model of Hansen and Coppens using the *Mopro* program. The experimental results are in close agreement with the theoretical values obtained after multipolar refinement using structure factors generated from DFT-D3 single point energy calculations. Strong electrostatic complementarity is found between contributing co-formers. The electron rich pyrazolone ring makes the carbonyl oxygen atom a strong acceptor of a classical hydrogen bond. Electrostatic interaction energies between **AN** and **CBA** molecules show one strong contribution of an **AN**–**CBA** dimer driving the cocrystallization and dictating the orientation of the coformers in the cocrystal. In general, the heterodimers between **AN**–**CBA** are more stable than the dimers between pure fragments. The topological analysis of intermolecular interactions shows that in addition to the single O–H···O hydrogen bond between **AN** and **CBA**, a large number of C–H···O and O–H···π type van der Waals interactions support the assembly. This study highlights the significance of using electrostatics to discuss the stability of crystalline solid forms of pharmaceutical cocrystals.

Received 28th August 2022,
Accepted 17th October 2022

DOI: 10.1039/d2ce01179d

rsc.li/crystengcomm

1. Introduction

Recent years have witnessed a tremendous increase in the pace of research related to improving the formulation of drugs that are lacking in physicochemical properties such as solubility,[1] stability,[2] flowability,[3] compressibility,[4] bioavailability,[5] and permeability.[6] Pharmaceutical co-crystallization is one of the solutions to these problems and has gained significant attention of the crystal engineering community. A pharmaceutical co-crystal[7–9] comprises of an active pharmaceutical ingredient (API) which is bonded with a physiologically acceptable molecule, 'the co-former' *via* non-covalent interactions.[10–12] There is a growing interest in the design of pharmaceutical co-crystals which depend on the availability of hydrogen bond acceptor and donor sites along with a deep understanding of the laws that govern the recognition of molecules based on supramolecular synthons.[13,14]

A knowledge-based approach[15] can be effectively used to design new solid forms of drugs. However, this requires a deep understanding of the nature of intermolecular interactions. Charge density analysis using highly diffracting crystals, ideally in centrosymmetric space groups, is a powerful method for evaluating non-covalent interactions, which not only play a vital role in supramolecular crystal engineering but also have an essential role in biological processes. Related electrostatic and topological analyses based on quantum theory of atoms in molecules (QTAIM)[16] are the ultimate tools to quantify the non-covalent interactions.

Antipyrine (**AN**), the first pyrazolone derivative synthesized by Ludwig Knorr in 1887 (ref. 17 and 18) has been used as an antipyretic, non-opioid analgesic, and anti-inflammatory drug.[19–22] AN tablets were once extensively used as pain reliever, however, due to some adverse effects such as allergic reactions, renal failure, respiratory problems, and gastric

[a] *Materials Chemistry Laboratory, Institute of Chemistry, The Islamia University of Bahawalpur, Baghdad-ul-Jadeed Campus, 63100, Pakistan. E-mail: maqsood.ahmed@iub.edu.pk*
[b] *Department of Chemistry and Biochemistry, Texas Christian University, Fort Worth, Texas, 76129, USA*
[c] *Laboratoire CRM2, UMR CNRS 7036, Université de Lorraine, Boulevard des Aiguillettes BP70239, Vandoeuvre-les-Nancy, 54506, France*
[d] *CNRS, Laboratoire CRM2, UMR CNRS 7036, Boulevard des Aiguillettes, BP70239, Vandoeuvre-les-Nancy, 54506, France*

† Electronic supplementary information (ESI) available. CCDC 2091231 and 2091232. For ESI and crystallographic data in CIF or other electronic format see DOI: https://doi.org/10.1039/d2ce01179d

hemorrhage,[23,24] it was discontinued in many countries. This drug, when consumed, acts on the central nervous system (CNS) leading to the non-selective inhibition of both isoforms of cyclooxygenase (COX-1, COX-2) enzymes which are involved in prostaglandin (PG) synthesis.[23,25,26] To date, several literature reviews focusing on antipyrine (API) co-crystals with suitable co-formers namely salicylic acid,[27] saccharin, fumaric acid,[28] 4-aminobenzoic acid,[29] sulphanilamide,[30] 4,4′-propane-2,2′-diyldiantipyrine[31] and sulfaguanidine[32,33] have been published. In addition, the literature also contains cocrystals of phenazone derivatives like propyphenazone–pyrithyldione,[34] propyphenazone–hydroquinone,[35] 4-aminoantipyrine-fumaric acid,[28] 4-aminoantipyrine-2-amino benzoic acid,[36] *etc.*; but no high-resolution study is available focusing on the electron density derived properties and the nature of intermolecular forces. An extensive search of the Crystallographic Structure Database[37] revealed that the carbonyl group of **AN** has high susceptibility to classical hydrogen bond formation with coformers containing carboxyl and amine functional groups. 2-Chlorobenzoic acid (**CBA**), a monocarboxylic acid acting as a proton donor, was therefore chosen as a suitable co-former based upon the predictability of hydrogen bonding.[38] This organic compound is strongly acidic compared to other isomeric forms of chlorobenzoic acid (2-chlorobenzoic acid, 3-chlorobenzoic acid, and 4-chlorobenzoic acid; pK_a values are 2.89, 3.9, and 3.98 respectively) and is generally used as a precursor to food additives, anti-inflammatory drugs, and dyes.[39–41]

Experimental charge density analysis using high resolution X-rays diffraction data provides a complete description of the electronic environment. Although the charge density analysis of small molecules is commonly available in the literature, it is still rare to find the charge density analysis of a cocrystal. The reason for this scarcity is the inherently weak diffraction by the cocrystals. An exhaustive literature survey provides the experimental electron-density analyses[42] of only a few co-crystals namely piroxicam–saccharin,[43] betaines-*p*-hydroxybenzoic acid,[44] melamine-barbital,[45] isonicotinamide-monofluorobenzoic acids,[46] nicotinamide-salicylic acid; nicotinamide-oxalic acid,[47] 8-hydroxyquinoline-salicylic acid,[48] sulfamethizole-oxalates/sulphates,[49] to have been successfully analysed, highlighting the challenges and importance of electron-density in better understanding of intermolecular interactions in crystalline solids.[50,51] In all of the above mentioned studies, the role of weak intermolecular interactions has been emphasized through a topological analysis highlighting their importance in stabilizing the cocrystal systems. Our group is currently working on the applications of charge density methods to cocrystals of those drug molecules.[52,53] Recently, we have also reported a co-crystal of nicotinic acid (an essential human nutrient also known as vitamin B3) with pyrogallol[54] and currently working on nicotinic acid-gallic acid co-crystal (Infal *et al.*, in review process).

In the present study, we report on an experimental charge density and electrostatic analysis of a new co-crystal of antipyrine with 2-chlorobenzoic acid, (**AN–CBA**) using a well diffracting crystal which allowed us to model the electron density distribution to a very reliable extent. It enabled us to gain insight into the covalent and non-covalent interactions and to calculate various electron density derived properties. The electrostatic properties of the non-covalent interactions combined with topological analysis of the electron density[16] enabled us to evaluate and rank their strength which is used to build the cocrystal. The experimental results have been compared with those obtained after multipolar refinement using theoretical structure factors calculated using periodic density functional theory (DFT) based calculations.

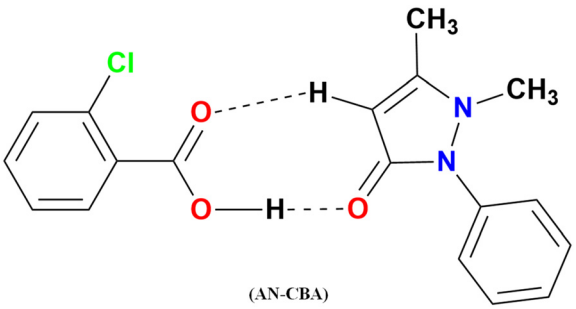

(AN-CBA)

2. Experimental

2.1. Material

Chemicals involved in this study, antipyrine (2,3-dimethyl-1-phenyl-5-pyrazolone) and 2-chlorobenzoic acid were acquired from a commercial supplier, and purity was checked using PXRD before use. Cocrystallization successfully takes place in various solvents however relatively better quality crystals were obtained in analytical grade ethanol.

2.2. Crystal growth

Antipyrine (0.094 g, 0.5 mM) and 2-chlorobenzoic acid (0.07 g, 0.5 mM) in 1 : 1 stoichiometric ratio were dissolved in ethanol. The solution was stirred for about 3 hours, poured into a glass vial, and left to evaporate slowly. Colourless block-shaped crystals of **AN–CBA** were obtained after a few days.

2.3. Data collection for SC-XRD analysis

High-resolution diffraction data were collected on a Bruker D8 Venture diffractometer with a PHOTON II detector[55] at 100 K using the 'Helios' focusing mirror optics to generate monochromatic Mo-K$_\alpha$ (λ = 0.71073 Å) radiation from a micro-focus source. After extensive screening, a suitably diffracting single crystal of dimension 0.29 × 0.23 × 0.11 mm^3 was used for data collection (Fig. S1†). The crystal was mounted on a glass needle using vacuum grease and then positioned on a four-circle goniometer. The temperature was cooled from room temperature to 100 K, using Oxford Cobra device from Oxford Cryosystems.[56] This device provided an excellent temperature stability of 0.1 K during the whole

course of the experiment. Two different exposure times of 10 s and 20 s per frame were set for low and high angle reflections respectively. Thus a total of 119 630 reflections were integrated with R_{int} of 0.051. Cell refinement and data reduction were done by SAINT software.[55] A numerical absorption correction was applied based on the real face indices of the crystal using the 'Index Crystal Faces' plugin in Apex3.[55]

2.4. PXRD analysis

PXRD analysis was performed using a Bruker D8 Advanced X-ray diffractometer with Cu K_α radiation (λ = 1.5406 Å) at ambient temperature. The X-ray tube was operated at 40 mA and 40 kV, respectively. The colourless crystalline sample was ground to a fine powder. The sample was scanned over a range of 6 to 80° (2θ) for co-crystals and 10 to 80° (2θ) for drug and co-former at a scan rate of 1 second/0.1°.

2.5. Thermal analysis

A simultaneous TGA/DSC analysis has been performed using Perkin Elmer STA 6000 to measure the thermal stability of the co-crystal formed. The sample of about 2 mg was heated at a rate of 10 °C min^{-1} to 500 °C. Nitrogen gas was used to purge the sample at a flow rate of 20 ml min^{-1}.

2.6. Structure solution and SHELX IAM refinement

The crystal structure of **AN–CBA** was solved in the monoclinic crystal system, space group $P2_1/c$ using direct methods. SHELXT[57] software was used for structure solution whereas an initial independent atomic model (IAM) refinement based on spherical atom approximation was performed using SHELXL.[58] The positions of all the H atoms could be located in the difference Fourier maps however a riding model[59] was used for the H-atoms attached to carbon atoms, Csp^2–H = 0.95 Å and Csp^3 – H = 0.98 Å. H atoms attached to the heteroatoms were refined freely.

2.7. *Mopro* IAM refinement

The refined model obtained from SHELXL was imported to the *Mopro* (*Mopro*_1805_win) software package.[60] First, a full-matrix least square refinement was carried out using the independent atomic model (IAM). In all refinement steps [$I > 2\sigma(I)$] threshold was used. The refinement results without a sigma cutoff on resolution are reported in the ESI.† Initially, the scale factor was refined using the whole resolution range then a high order refinement ($\sin\theta/\lambda \geq 0.8$ A^{-1}) was carried out for all non-hydrogen atoms. The position of the H atoms attached to the C and O atoms were constrained to those obtained from a standard periodic DFT-D3 optimized geometry (Table S1†). The anisotropic displacement parameters for H atoms were constrained to the values calculated from the SHADE server.[61] The Cl1 atom was modelled using an anharmonic thermal motion description up to the third order of the Gram–Charlier expansion, resulting in some improved residual density maps.[62] At the end of IAM refinement, the scale factor was again refined using complete data to calculate dynamic deformation electron density maps (Fig. 1 and S2†); the quality of these maps encouraged us to proceed with a multipolar model.

2.8. Multipolar atom model refinement

The charge density of **AN–CBA** was subsequently refined against F^2 using multipolar scattering formalism of Hansen & Coppens[63] *via* *Mopro* program.[60] According to this formalism, the pseudo-atom electron density in a molecule is defined as:

$$\boldsymbol{\rho}(\boldsymbol{r}) = \rho_{core}(r) + P_{val}\kappa^3\rho_{val}(\kappa r) + \sum_{l=0}^{l_{max}} \kappa'^3 R_{n_l}(\kappa' r) \sum_{m=0}^{l} P_{lm}\, y_{lm\pm}(\theta,\varphi)$$

where the first two terms represent the core and the valence electron densities of an atom, respectively. The last term corresponds to the aspherical part of electron density projected on real spherical harmonics. P_{val} is the valence shell population and $P_{lm\pm}$ are multipole populations whereas

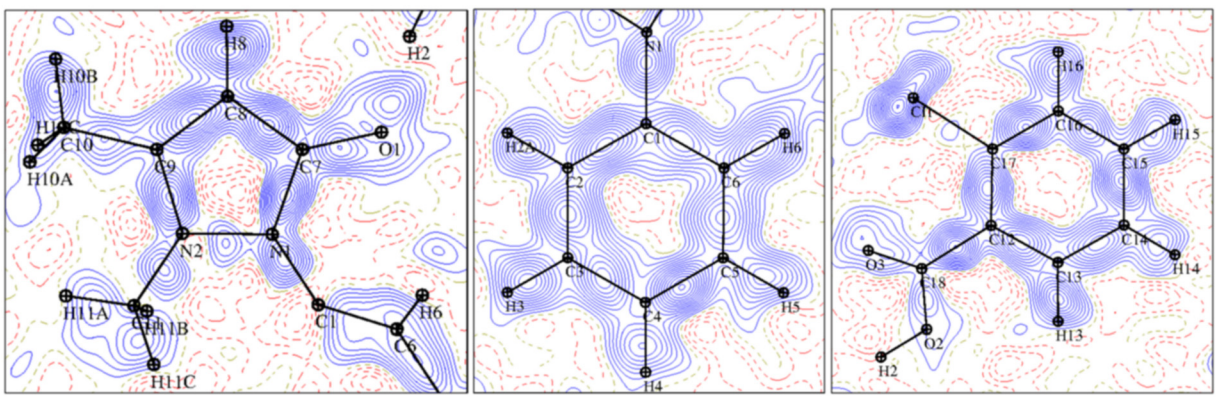

Fig. 1 Dynamic deformation electron density maps (*Moproviewer*) of the molecular complex (**AN–CBA**) after IAM refinement with *Mopro*; contour level of 0.05 e $Å^{-3}$ and with $\sin\theta_{Max}/\lambda$ = 0.7 $Å^{-1}$.

κ and κ' are the coefficients for contraction/expansion in the valence shell. R_l is radial slater-type function.

The multipolar refinement was carried out using diffraction data up to ($\sin\theta/\lambda$ = 0.95 A^{-1}) using reflections with I/σ >2 while S3 reports refinement results using data without any I/σ cutoff. It was carried out in systematic steps and chemical constraints based on hybridization, atom type, and chemical environment (Table S2†) were imposed in the initial stages of refinement: firstly the valence population (P_{val}) was refined together with the scale factor, followed by the refinement of spherical κ, multipoles (P_{lm}), and multipolar κ' for all atoms. The multipoles were truncated at dipolar level for the hydrogen atoms, octapolar level for C, N, and O and hexadecapolar level for chlorine. The κ and κ' parameters for the hydrogen atoms were restrained to 1.16(2). The condition of charge neutrality was maintained during multipolar refinement and in later stages of refinement; symmetry equivalent and chemical constraints were gradually lifted to ensure model stability. All parameters (scale, positional and anisotropic displacement parameters, P_{val}, P_{lm}, κ and κ') were refined together in the last cycles to achieve convergence. Residual electron density maps of MM_{exp}, and MM_{theo} are shown in Fig. 2 (Fig. S2†) and refinement statistics are enlisted in Table 1, the maps are clean although some peaks (0.15 e A^3) remain close to some methyl H atoms. There is a qualitative agreement between theoretical and experimental values, though the values obtained from experimental model are systematically higher. Refinement with all data (Table S3 in ESI†) is in line with those discussed above and does not improve the model. We then decided to discuss the stability of the cocrystal based on the I/σ > 2 levels as many authors currently do.[64–67]

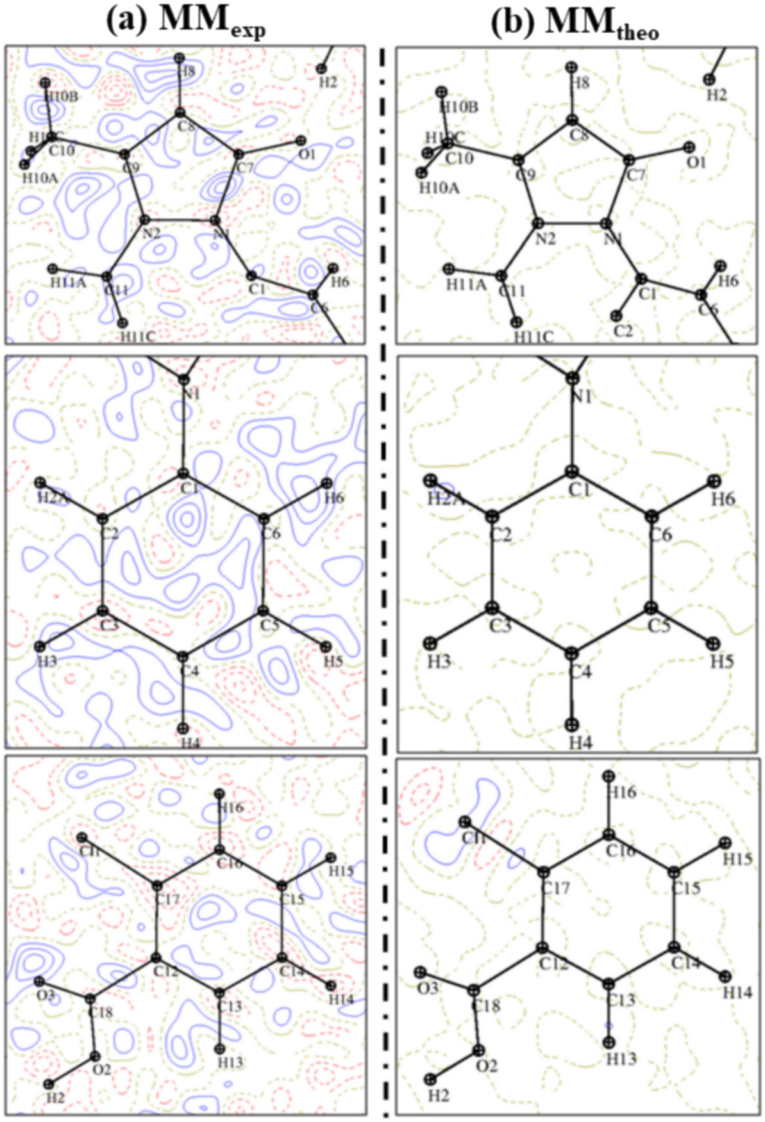

Fig. 2 Fourier residual electron density of the molecular complex (**AN–CBA**) after MM_{exp} and MM_{theo} refinement at contour level of 0.05 e $Å^{-3}$ with $\sin\theta/\lambda$ = 0.7 $Å^{-1}$.

Table 1 Crystallographic refinement details of **AN–CBA**

Crystal data			
Chemical formula	$C_{18}H_{17}ClN_2O_3$		
M_r	344.77		
Crystal system, space group	Monoclinic, $P2_1/c$		
Temperature (K)	100(1)		
a, b, c (Å)	12.4003(3), 7.1632(1), 18.4777(4)		
β (°)	92.6750 (1)		
V (Å^3)	1639.51(5)		
Z	4		
Radiation type	Mo K (λ = 0.71073 Å)		
μ (mm^{-1})	0.252		
Crystal size (mm)^3	0.29 × 0.23 × 0.11		
Data collection			
Diffractometer	Bruker D8 Venture with PHOTON II detector		
Absorption correction	Numerical[55]		
T_{min}, T_{max}	0.977, 0.991		
Total number of reflection measured/independent	119 630/13 656		
R_{int}	0.0509		
$(\sin\theta/\lambda)_{max}$ (Å^{-1})	0.95		
Refinement	**IAM**	**Multipolar**	**Theoretical**
Refinement based on	F^2	F^2	F
$R[F^2 > 2\sigma(F^2)]$, w$R(F^2)$, S	0.061, 0.179, 1.00 (high order)	0.043, 0.031, 1.04	0.006, 0.007, 0.23 (0.95 Å^{-1}) $R[F]$, w$R(F)$, S 0.005, 0.005, 0.08 (1 Å^{-1})
No. of reflections used	9233 [$I > 2.0\sigma(I)$]	9233 [$I > 2.0\sigma(I)$]	9233 (0.95 Å^{-1}) 13 519 (1 Å^{-1})
Weighting scheme	$\sigma w^2 = (a\text{sig}Y_o^2 + bF_o^2)$ where a = 1.38951 and b = 0.00045	$\sigma w^2 = (a\text{sig}Y_o^2 + bF_o^2)$ where a = 1.38951 and b = 0.00045	$\sigma w^2 = (a\text{sig}Y_o^2 + bF_o^2)$ where a = 0.50 and b = 0.00007
No. of parameters	217	804	435
$\Delta\rho_{min}$, $\Delta\rho_{max}$ (e Å^{-3})	−0.42, 0.75	−0.37, 0.38	−0.28, 0.34 (0.95 Å^{-1})

2.9. Computational details

We performed two types of periodic density functional theory (DFT) calculations:

(i) Initially, the optimization of atomic positions of hydrogen atoms was carried out using periodic DFT-D3 calculations starting with the lattice parameters and atomic positions obtained from *Mopro* IAM refinements converged with the standard neutron distances. During the partial geometry optimization, the coordinates of all non-hydrogenic atoms in the unit cell were fixed and only hydrogen atoms were allowed to relax until convergence. The convergence criteria on forces and threshold on total energy was set to less than 10^{-4} (a.u) and 10^{-7} (a.u), respectively. The calculations use Quantum-Espresso[68] (QE) suites of programs. Ultrasoft pseudopotentials were used for all atoms using the Perdew–Burke–Ernzerhof (PBE)[69] exchange–correlation functional in combination with Grimme's D3 correction for dispersion interactions.[70] We set the cutoff energy and electronic density of plane-waves to 60 Ry and 675 Ry respectively, established after running various cutoff tests. The mesh of the unit cell for k-point sampling was set to 5 × 9 × 3 which corresponds to ~0.1/Å of k-space resolution. A mixing factor of 0.7 was used to achieve the self-consistency. We use the obtained optimized hydrogen distances for further *Mopro* IAM and subsequently, for the multipolar refinements.

(ii) In the second stage, a DFT-D3 single point energy calculation was performed on the final coordinates obtained after the multipolar refinement by using all-electron frozen-core PAW[71] methodology on a dense real-space grid comprising of 360 × 180 × 432 points along the crystallographic axes. The PBE exchange–correlation approximation was used with the same k-point sampling used for partial geometry optimization. The theoretical structure upto $\sin\theta/\lambda$ limits of 0.95 Å^{-1} were obtained by the Fourier transform of the obtained total electron density grid by using a Python script developed by one of us (AM). Multipolar refinement of scale-factors and electron density parameters was performed using the obtained static structure factors by excluding the refinement of atomic positions while thermal parameters of atoms were set to zero. The results of the refinement are mentioned as "MM_{theo}" in all subsequent studies.

A fractal dimensions plot comparing the residual densities after multipolar refinements has been given in Fig. S3† which shows the results are comparable.

3. Results and discussion

3.1. Powder X-rays diffraction analysis

The PXRD pattern of **AN–CBA** (as illustrated in Fig. S4†) differs from the starting materials with characteristic peaks

of co-crystal at 14.40°, 19.97°, 23.18° and 27.40° ($\sin\theta/\lambda$ = 0.18, 0.24, 0.28, 0.33 respectively) while pure antipyrine drug shows characteristic peaks at 11.61°, 19.94° and 23.57° ($\sin\theta/\lambda$ = 0.14, 0.24, 0.29 respectively). Similarly, 2-chlorobenzoic acid exhibits characteristic peaks at 15.02°, 22.66° and 30.40 ($\sin\theta/\lambda$ = 0.18, 0.28, 0.37 respectively). This diffraction pattern confirms that the cocrystal is a distinct new crystalline phase. The PXRD pattern of co-crystal is comparable to the simulated pattern generated from crystal structure using *Mercury*[72] which confirms its purity.

3.2. TGA/DSC analysis

The thermogram with DSC curve of co-crystal (**AN–CBA**) is shown in Fig. S5.† The sharp weight loss during the experiment indicates the loss of water or solvent molecules and also indicates the decomposition of co-crystal.[73,74] It shows that the co-crystal is stable up to 140 °C and a complete weight loss is observed at endothermic peaks of 246.85 °C respectively. In comparison with the pure drug (antipyrine), the co-crystal shows a decrease in thermal stability by about 15–20 °C.

3.3. Crystal structure and geometry

In the current study, the co-crystal structure of a new solid form (**AN–CBA**) was determined at low temperature for charge density studies. The **AN–CBA** crystallizes in the monoclinic system with space group $P2_1/c$. The thermal displacement ellipsoids of the asymmetric unit with atom numbering scheme drawn with *MoproViewer*[75] are shown in Fig. 3. In the crystal structure, the methyl group of **AN** deviates from the pyrazolone plane with C-methyl slightly deviating by 0.09 Å while the N-methyl group is significantly out (0.571 Å) due to steric hindrance. Additionally, in terms of Roumanos and Kertesz[76] criteria, the φ, α and β (64.94°, 30.8° and 326.09° respectively) are in an allowed range and no outlier was observed, however, the conformation of antipyrine in the **AN–CBA** cocrystal was observed to have undergone a change (Fig. S6†) from DU (down-up, pure drug) to UD (up-down). This can be attributed to a weak C2···H11C (bond length = 2.6048 Å) intramolecular interaction (Fig. S7†). Similarly, the COOH functional group connected to the benzene ring *via* C–C exocyclic bond makes a dihedral angle of 36.17° possibly due to intramolecular halogen O3···Cl1 (2.989 Å). Table S4† lists the topological parameters of all covalent bonds; they are in close agreement with the literature. This confirms the quality of the data and the multipolar refinement. Furthermore, all experimental topology parameters agree well with the theoretical values although the later values are slightly but systematically lower than the experimental values.

The geometric analysis and molecular packing of **AN–CBA** give insight into the cocrystal's stability. The **AN** and **CBA** in the asymmetric unit are interconnected through a conventional O2–H2···O1 hydrogen bond and a weak C8–H8···O3 van der Waals interaction forming a ring motif $R_2^2(8)$, as indicated in Fig. 3. The neighbouring molecules are linked *via* C14–H14···O1^{ii} and C13–H13···O2^{ii} hydrogen bonds involving H atoms of the **CBA**-phenyl ring and the carbonyl as well as carboxyl groups O atoms to generate a tetrameric assembly. The adjacent tetramer makes a one-dimensional layer along the crystallographic 2_1-screw axis (*b*-axis) joined through weak C10–H10C···O1^{v} interaction (Fig. 4b). This tetrameric-1D layer, as illustrated in Fig. 4c, further makes an extensive 3D layered network governed by weak C–H···O and C–H···C interactions. Table 2 gives the list of these strong and weak hydrogen bonds with respective symmetric codes.

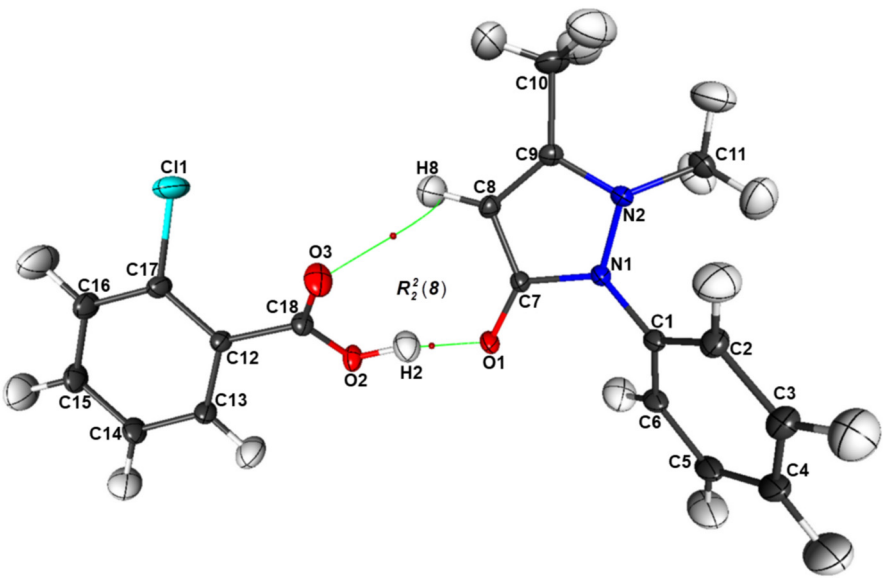

Fig. 3 A thermal ellipsoid plot of co-crystal (**AN–CBA**) drawn at a probability of 50% with atom numbering scheme for atoms, showing a ring motif with graphical set notation $R_2^2(8)$.[77]

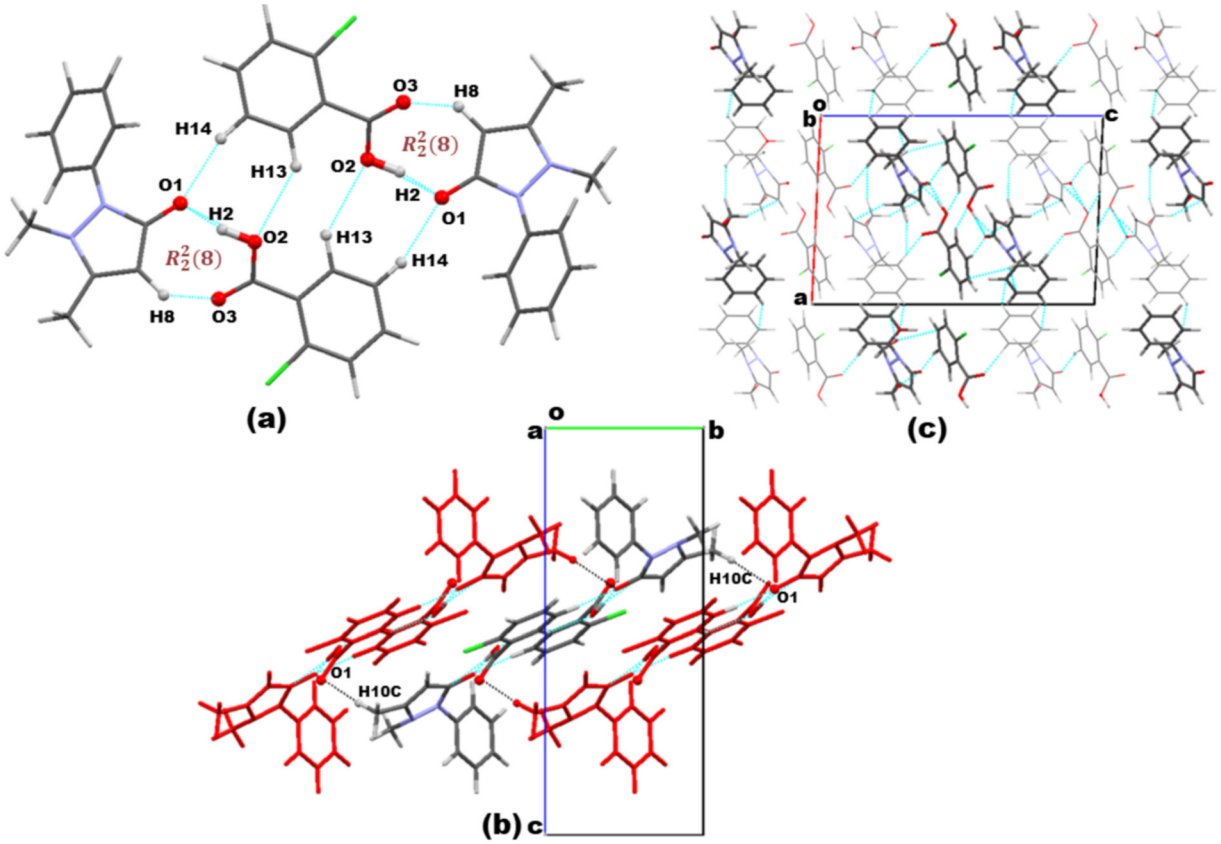

Fig. 4 A view of packing arrangement in co-crystal (**AN–CBA**). (a) Tetrameric assembly of **CBA** with **AN**, (b) 1D layer long *a*-axis linked *via* C10–H10C···O1^{v} interaction (black dotted lines) and (c) 3D network along *b* axis showing weak interaction. Symmetry codes are given in Table 2.

An analysis of the colour coded Hirshfeld surface (Fig. 5);[78–80] generated using *Crystal Explorer17* (ref. 81) also shows that weak C10–H10A···C8^{i}, C13–H13···O2^{ii}, C14–H14···O1^{ii}, C8–H8···O2^{iii}, C4–H4···C6^{iv} and C10–H10C···O1^{v} interactions are present in the crystal structure (symmetry codes are given in Tables 2 and 5). Areas in the blue indicate contact distances longer than the sum of the van der Waals radii while those in the white show contact distances equal or just equal to the sum of van der Waal's radii. The surface lacks regions where contact distances are shorter than the sum of the van der Waal's radii. The fingerprint plots mapped with d_{norm} (ref. 82) showing the percentage contribution to the surface has been given in Fig. S8.† These weak interactions participating in cocrystal assembly are quantitatively

Table 2 Hydrogen-bond geometry (Å, °) for **AN–CBA**

D–H···A	D–H	H···A	D···A	D–H···A
O2–H2···O1	1.05	1.51	2.5487 (6)	169 (8)
C8–H8···O3	1.08	2.70	3.256 (2)	112 (4)
C11–H11C···C2	1.09	2.61	3.2202 (9)	115 (1)
C10–H10A···C8^{i}	1.10	2.58	3.5467 (10)	146 (6)
C13–H13···O2^{ii}	1.09	2.62	3.5238 (8)	141 (4)
C14–H14···O1^{ii}	1.09	2.32	3.3662 (8)	160 (6)

Symmetry codes: (i) $-x+1, y-1/2, -z+1/2$; (ii) $-x+1, -y, -z+1$; (iii) $-x+1, -y+1, -z+1$; (iv) $-x, y+1/2, -z+1/2$; (v) $x, y-1, z$; (vi) $-x+2, -y+1, -z+1$.

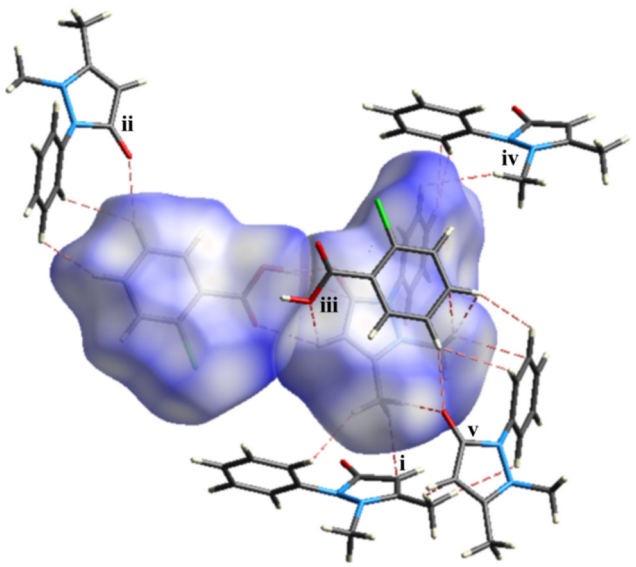

Fig. 5 Individually calculated Hirshfeld surface of each fragment in **AN–CBA**, with various neighbouring species interacting with them. Areas in the blue indicate contact distances longer than the sum of the van der Waals radii while areas in the white show contact distances equal or just shorter than the sum of the van der Waal's radii.

Table 3 Atomic charges (e) and atomic volume (Å^3) of co-crystal **AN**–**CBA**. MM denotes multipolar model while 'exp' and 'theo' represents experimental and theoretical results

	MM_{exp}		MM_{theo}	
Atoms	Charge (q)	Volume (Å^3)	Charge (q)	Volume (Å^3)
Cl1	−0.209	33.60	−0.250	34.56
O3	−1.184	18.80	−0.963	18.06
O1	−1.172	16.90	−0.905	16.11
O2	−1.274	16.83	−1.019	16.18
C11	−0.531	14.39	0.094	9.83
C3	−0.155	13.32	−0.059	13.27
C2	−0.118	13.24	−0.053	12.88
C16	−0.222	12.79	−0.041	11.82
C10	−0.372	12.72	−0.073	11.06
C13	−0.104	12.48	−0.047	12.40
C5	−0.148	11.82	−0.061	11.67
C6	−0.117	11.65	−0.078	11.53
C8	−0.141	11.60	0.046	11.14
C14	−0.005	11.59	−0.066	12.09
C4	0.011	11.26	−0.055	11.82
C15	0.105	11.07	−0.051	11.55
N1	−0.762	10.62	−0.547	10.30
C12	−0.112	9.85	0.004	9.41
N2	−0.663	9.62	−0.534	9.56
C17	0.125	9.37	0.070	9.86
C1	0.274	8.96	0.213	9.46
C9	0.601	7.79	0.241	8.62
H8	0.167	7.64	0.128	7.61
H6	0.125	7.61	0.096	7.27
H15	0.122	7.55	0.063	7.57
H5	0.124	7.37	0.060	7.58
H4	0.114	7.00	0.070	7.01
H16	0.140	6.98	0.083	7.13
H10B	0.136	6.95	0.072	7.49
H3	0.123	6.81	0.065	6.85
H14	0.118	6.74	0.109	6.60
H13	0.131	6.60	0.097	6.86
H10C	0.136	6.59	0.080	7.07
C7	1.011	6.33	0.881	7.01
H11A	0.398	6.10	0.100	6.98
H10A	0.132	6.09	0.082	6.43
H2A	0.127	5.83	0.090	5.85
H11B	0.395	5.12	0.051	6.56
H11C	0.397	5.06	0.098	6.22
C18	1.653	4.76	1.370	5.64
H2	0.637	1.57	0.552	2.09

characterised based on electrostatic and topological analysis in section 3.5.

3.4. AIM atomic charges and volumes

The atomic charges are calculated as the difference between the sum of electronic and nuclear charges at the atomic basins. The boundary of the atomic basin is defined as zero flux surfaces which is usually a thick solid line.[83,84] The integration of electron density to obtain the atomic charges and volumes from both experimental and theoretical refinement models was performed by using *WinXPRO*[85] suite and are listed in Table 3. Both the experimental and theoretical values are well correlated and compatible with the chemical environment. As expected the oxygen atoms have the highest values of negative charge (−1.2 e in average) and are thus involved in the strongest interactions between **AN** and **CBA**. The basic N atoms in the pyrazalone ring are also strongly negative (N1, experimental −0.762/theoretical (0.95 Å^{-1}) −0.547 e and N2, −0.663/−0.534) in agreement with their electron withdrawing character. These charges have noticeable effect on the charges of the pyrazalone atoms. An alternation of large positive/negative AIM charges is observed along the ring: for example, the C7 atom charge is +1.0 e bound *via* highly polar bonds to three negative atoms (O1, N1, and C8). C7 AIM volume (6.3/7.01 A^3) is small similar to that of an H atom. The Cl atom carries a negative charge of −0.209/−0.250 e much lower than the electronegative atoms (O & N). The hydroxyl H2 atom (0.637/0.552 e) carries a relatively higher positive charge compared to the carbon-bonded H atom which confirms the acidic character of the resultant atom (positive charge and smallest atomic basin; Fig. S9†) and displays binding affinity. A net charge transfer of 0.08 electron was noticed to have been transferred from **AN** to **CBA** moiety.

3.5. Analysis of the intermolecular interactions, electrostatic potential electrostatic interaction energies and topology of the electron density

The analytical form of the multipolar electron density of the AB cocrystals enables to calculate local properties such as intermolecular topological properties at the critical point,[16] and non-local ones such as electrostatic potential generated by A or B, electric field, electrostatic energy between interacting molecules.[86–92] These complementary calculations are needed to rank the interactions and to propose a mechanism for cocrystal growth.[54] It is important for the stability of AB cocrystals to see how the electrostatic potential generated by the A sublattice is complementary to that generated by B and *vice versa*.

Electrostatic potential is one of the most important properties to describe interactions in the solid state. It exhibits the electrophilic (positive potential) and nucleophilic (negative potential) regions of the molecule and is a good indicator of the chemical reactivity.[93,94] The electrostatic potential can be directly calculated from the multipolar electron density using the following relation

$$V(r) = \sum_{A} \frac{Z_A}{|R_A - r|} - \int \frac{\rho(r')}{|r' - r|} dr'$$

Z_A is the charge of nucleus A situated at a distance R_A and ρ is the total electron density.[95] Furthermore, the electrostatic interaction energies between molecular dimers can be calculated by Buckingham summation[96] and provide important insight into the initiation of the cocrystallization and subsequent packing stability of the cocrystal assembly. The literature contains several examples where the electrostatic interaction energy has been used to understand binding and interactions not only in small molecule's crystal environment but also between protein–ligand complexes.[86–92]

Therefore we have calculated the electrostatic potential and electrostatic interaction energy using the following equation (with *Moproviewer*) to understand how the cocrystallization onsets and why the cocrystal remains stable.

$$E^{A,B} = \int \rho^{A}(\vec{r}) V^{B}(\vec{r}) d\vec{r}$$

and *vice versa*. Furthermore, the topological analysis based on electron density using Bader's quantum theory of atoms in molecule, QTAIM[16] in the **AN** and **CBA** molecules is useful to quantify the individual covalent and non-covalent interactions.

a) Major interaction in the crystal. As discussed above the strongest interaction stabilizes the **AN–CBA** dimer (called hereafter reference dimer) of the asymmetric unit *via* the O2–H2···O1 hydrogen bond. Fig. 6a and b show the 3D electron density surface of the **AN** and **CBA** molecules coloured according to the electrostatic potential they generate. These are the potentials of the molecules removed from the crystal lattice. The **AN** moiety is highly polar in nature with a dipole moment of 13.45D (Fig. S10†). On its iso surface, the negative potential is concentrated on the O1 oxygen atom but also spread in its vicinity. On the other hand, the **CBA** moiety is less polar with a dipole moment of 7.02D (Fig. S10†) with a negative potential spread over a wider region. It contains three pockets of negative potential, around two carboxyl oxygen atoms and one on the chlorine atom. A strong positive potential is observed on the H2 atom attached to the hydroxyl O2 atom of CBA. This positive potential of the H2 atom is complementary to the negative potential of O1. Fig. 6c shows the electrostatic potential when AN and CBA interact to form the reference dimer. As expected, this interaction neutralizes the H2 positive potential and the resulting potential is smoother reducing the electric field in this region. Similarly, the strong negative potential of the O3 atom (CBA) is complemented by the positive potential of the H8 atom of AN and the methyl groups of a neighbouring AN^{i}. (i) $-x + 1$, $y - 1/2$, $-z + 1/2$; it is thus evident that the orientation and packing are primarily dictated by the quasi neutralization of the negative potentials of the three oxygen atoms, foremost being that of O2–H2···O1 region as evident from Fig. 6c.

Table 4 lists the electrostatic interaction energies between all stable molecular **AN–CBA** dimers in the cocrystal. The experimental values for energies are systematically higher than the theoretical values despite their net charges are very close to each other (Table S6†). This difference can be attributed to a higher electrostatic potential for experimental as shown by a stronger contrast in Fig. S17.† However, the hierarchy of the interaction energies remains the same. The reference dimer discussed above possesses the highest value of the interaction energy owing to the presence of the only strong O–H···O hydrogen bond of this cocrystal system which is further strengthened by a C–H···O interaction. These values can be compared to those recently calculated for the nicotinic acid–pyrogallol (**NA–PY**) cocrystal between highly polar zwitterionic nicotinic acid moieties.[54]

Tables 5 and S5† list the topological parameters of the non-covalent interactions calculated using *VMopro*[60] and *Moproviewer*.[75] Most interactions meet the first four of Koch and Popelier's criteria which are considered necessary and sufficient for an interaction to be a hydrogen bond.[97,98] The topological analysis (Table S5†) of the O2–H2···O1 hydrogen bond which builds the reference **AN–CBA** dimer shows a large value of the electron density at the critical point (experimental/theoretical (0.95 Å^{-1}) 0.426/0.410 e A^{-3}). This strong interaction also possesses the highest stabilizing value of potential (−204/−194 kJ per mole) and kinetic energy (+182/+177 kJ per mole) densities at CP with E_{CP} = −22/−17 kJ per mole. In conclusion, from electrostatic and topological analyses, it is clear that there is only one strong interaction forming the **AN–CBA** reference dimer. It provides the initial synthon for the onset of cocrystallization. Any other **AN–CBA** polymorph, if it exists, should grow from this reference dimer.

b) Weak interactions in the cocrystal. Further inspection of Table 4 shows that the second hetero dimer (**AN**···**CBA**^{i}) has an energy considerably less compared to the reference dimer as it is involved in three weaker C–H···O and C–H···π interactions. One of the hydrogen atoms among these C–H···O interactions is donated by the C2 carbon atom of the phenyl ring while the other H10C is donated by the methyl carbon (C10). The acidic character of the aromatic and methyl hydrogen atoms is also evident from the electrostatic potential maps (Fig. 6). Subsequently, one finds alternatively **AN–AN** and **AN–CBA** interactions with successively decreasing values of electrostatic energies as these dimers interact *via*

Table 4 Electrostatic interaction energies of the molecular dimers in the cocrystal, **AN–CBA**. Theoretical values are given in italic: second row (0.95 Å^{-1})

Interactions		Electrostatic energy values (kJ mol^{-1})
O2–H2···O1	AN···CBA	−129
C8–H8···O3		*−81.5*
C2–H2A···O3^{i}	AN···CBA^{i}	−49.2
C3–H3···C16^{i}		*−28.7*
C10–H10A···O3^{i}		
C10–H10C···O1^{v}	AN···AN^{v}	−47.9
		−20.3
C14–H14···O1^{ii}	CBA···AN^{ii}	−29.7
		−10.2
C4–H4···C6^{iv}	AN···AN^{iv}	−10.7
		−6.66
C10–H10C···O2^{v}	AN···CBA^{v}	−9.34
C10–H10B···O3^{v}		*−2.89*
C10–H10A···C8^{i}	AN···AN^{i}	−1.28
		4.35
C13–H13···O2^{ii}	CBA···CBA^{ii}	−0.116
		0.325
C8–H8···O2^{iii}	AN···CBA^{iii}	38.0
C6–H6···C16^{iii}		*−5.69*

Symmetry codes: (i) $-x + 1$, $y - 1/2$, $-z + 1/2$; (ii) $-x + 1$, $-y$, $-z + 1$; (iii) $-x + 1$, $-y + 1$, $-z + 1$; (iv) $-x$, $y + 1/2$, $-z + 1/2$; (v) x, $y - 1$, z; (vi) $-x + 2$, $-y + 1$, $-z + 1$.

Table 5 Topological parameters at critical points in **AN–CBA**, obtained from the multipolar refinement of experimental (first row) and theoretical data (second row 0.95 Å^{-1}: electron density (e Å^{-3}), Laplacian (e Å^{-5}), ε = ellipticity, G_{CP} = bond kinetic-energy density (kJ mol^{-1} Bhor^{-3}), V_{CP} = bond potential-energy density (kJ mol^{-1} Bhor^{-3}), $|V_{cp}|/G_{cp}$ and total electronic energy density, E_{cp} (kJ mol^{-1} Bohr^{-3}))

Interactions		ρ_{BCP} (r)	$\nabla^2\rho$ (BCP)	ε	G_{CP}	V_{CP}	$\lvert V_{cp}\rvert/G_{cp}$	E_{cp}
O2–H2···O1	AN···CBA	0.425 (3)	5.88	0.009	182	−204	1.12	−22.0
		0.410 (1)	5.86	0.008	177	−194	1.10	−17.5
C10–H10A···C8^{i}	AN···AN^{i}	0.058 (1)	0.759	0.402	16.5	−12.4	0.748	4.16
		0.059 (1)	0.779	0.409	16.9	−12.7	0.749	4.26
C14–H14···O1^{ii}	CBA···AN^{ii}	0.057 (1)	1.16	0.007	23.7	−15.8	0.667	7.90
		0.059 (2)	1.16	0.012	23.9	−16.2	0.677	7.73
C8–H8···O2^{iii}	AN···CBA^{iii}	0.051 (2)	0.752	0.080	15.9	−11.2	0.708	4.05
		0.045 (3)	0.694	0.141	14.4	−9.89	0.687	4.09
C8–H8···O3	AN···CBA	0.043 (1)	0.628	0.209	13.0	−9.00	0.689	4.05
		0.040 (1)	0.613	0.149	12.6	−8.51	0.675	4.09
C13···C8 (pi–pi interaction)	CBA···AN	0.040 (2)	0.467	6.900	9.99	−7.26	0.727	2.73
		0.042 (1)	0.484	3.110	10.4	−7.57	0.730	2.80
C4–H4···C6^{iv}	AN···AN^{iv}	0.039 (1)	0.539	0.516	11.2	−7.70	0.688	3.49
		0.039 (2)	0.562	0.324	11.7	−7.99	0.686	3.66
C10–H10C···O2^{v}	AN···CBA^{v}	0.037 (4)	0.519	1.770	10.7	−7.32	0.682	3.41
		0.035 (4)	0.513	1.38	10.5	−7.05	0.670	3.46
C10–H10B···O3^{v}	AN···CBA^{v}	0.035 (4)	0.489	0.261	10.1	−6.83	0.678	3.24
		0.032 (3)	0.466	0.305	9.49	−6.28	0.661	3.21
C10–H10C···O1^{v}	AN···AN^{v}	0.035 (1)	0.731	0.268	14.4	−8.98	0.621	5.46
		0.033 (1)	0.721	0.284	14.1	−8.67	0.613	5.48
C13–H13···O2^{ii}	CBA···CBA^{ii}	0.034 (1)	0.613	0.102	12.2	−7.81	0.638	4.44
		0.033 (2)	0.603	0.001	12.1	−7.69	0.638	4.37
C2–H2A···C12^{i}	AN···CBA^{i}	0.033 (3)	0.429	0.523	8.83	−5.97	0.676	2.86
		0.032 (1)	0.442	0.429	9.04	−6.04	0.668	3.00
C2–H2A···O3^{i}	AN···CBA^{i}	0.031 (4)	0.635	0.183	12.5	−7.73	0.618	4.78
		0.030 (2)	0.623	0.473	12.2	−7.50	0.613	4.74
C3–H3···C16^{i}	AN···CBA^{i}	0.030 (3)	0.401	0.963	8.18	−5.43	0.664	2.75
		0.029 (2)	0.422	1.942	8.56	−5.62	0.657	2.94
C11–H11C···C5	AN···AN	0.029 (1)	0.312	0.632	6.51	−4.53	0.696	1.98
		0.023 (2)	0.337	0.398	6.69	−4.21	0.629	2.48
Cl1···H14^{v}	CBA···CBA	0.028 (1)	0.347	−0.06	0.49	−0.06	0.122	0.43
		0.030 (3)	0.370	−0.06	0.50	−0.06	0.120	0.44
C10–H10A···O3^{i}	AN···CBA^{i}	0.024 (2)	0.448	0.025	8.78	−5.36	0.610	3.42
		0.024 (4)	0.432	0.251	8.51	−5.25	0.617	3.26
Cl1···H3^{i}	CBA···AN	0.021 (4)	0.283	0.110	5.66	−3.63	0.641	2.03
		0.024 (2)	0.309	0.279	6.26	−4.10	0.655	2.16
Cl1···H16^{vi}	CBA···CBA	0.020 (2)	0.395	0.032	7.67	−4.56	0.595	3.11
		0.024 (3)	0.426	0.006	8.38	−5.15	0.615	3.23
C15–H15···C3	CBA···AN	0.018 (3)	0.275	0.730	5.39	−3.29	0.610	2.10
		0.019 (4)	0.278	1.04	5.51	−3.44	0.624	2.07
C6–H6···C16^{iii}	AN···CBA^{iii}	0.017 (3)	0.233	0.633	4.59	−2.83	0.617	1.76
		0.016 (4)	0.223	0.984	4.35	−2.63	0.605	1.72
Cl1···Cl1^{vi}	CBA···CBA^{vi}	0.010 (2)	0.149	1.96	2.87	−1.68	0.585	1.19
		0.013 (1)	0.190	1.27	3.37	−2.28	0.677	1.09

Symmetry codes: (i) $-x+1, y-1/2, -z+1/2$; (ii) $-x+1, -y, -z+1$; (iii) $-x+1, -y+1, -z+1$; (iv) $-x, y+1/2, -z+1/2$; (v) $x, y-1, z$; (vi) $-x+2, -y+1, -z+1$.

van der Waal's type of interactions. The topological analysis of all these interactions (Table S5†) shows that the electron density at the CP is much smaller, less than 0.06 e Å^{-3} while the kinetic and potential energy densities are less than 17 and −13 kJ mol^{-1} Bohr^{-3}, respectively. Additionally, weak Cl···H interactions occur with a bond length (d_{12}) from 3 to 3.28 Å (longer than the sum of VdW radii 2.95 Å) with average $\nabla^2\rho$(BCP), $|V_{cp}|/G_{cp}$ and E_{cp} of 0.34/0.37 e Å^{-5}, 0.45/0.46 kJ mol^{-1} Bohr^{-3}, and 1.85/1.94 kJ mol^{-1} Bohr^{-3} respectively. Critical points with ρ_{cp} = 0.01–0.028 e Å^{-3} are observed for a couple of Cl···Cl interactions although the interaction length ($d_{12} \geq 4$ Å) is much longer than sum of VdW radii 3.5 Å (Table 5, Fig. S16†). All the intermolecular interactions described above fulfill the criterion $\nabla^2\rho(\text{BCP}) > 0$, $|V_{cp}|/G_{cp} < 1$, and $E_{cp} > 0$ (ref. 99 and 100) and are effective as closed-shell interactions. Although, all these weak interactions are mainly the result of the crystal packing but their role in the stability of the cocrystal cannot be ignored.

One hetero dimers (**AN**···**CBA**^{iii}) (symmetry code: (iii) $-x+1, -y+1, -z+1$) has a sizeable value of positive electrostatic interaction energy (37.96 kJ per mole) and therefore can be considered as destabilizing. The repulsive behavior becomes evident viewing the electrostatic potential maps (Fig. 7) where regions with negative potential (shown in red) come face to

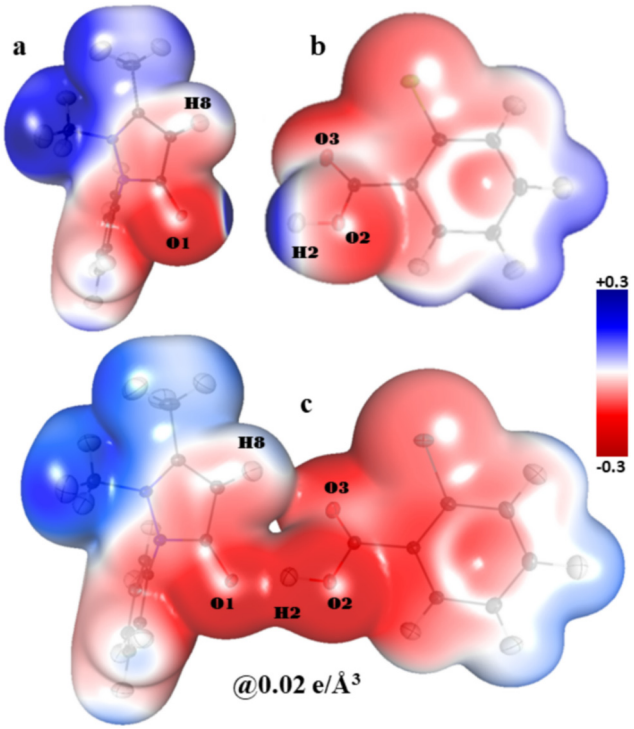

Fig. 6 Three-dimensional electron density surfaces of **AN** (a) **CBA** (b) and the co-crystal **AN–CBA** (c) dimer (experimental) generated at isosurface value of 0.02 e $Å^{-3}$ coloured according to the electrostatic potential.

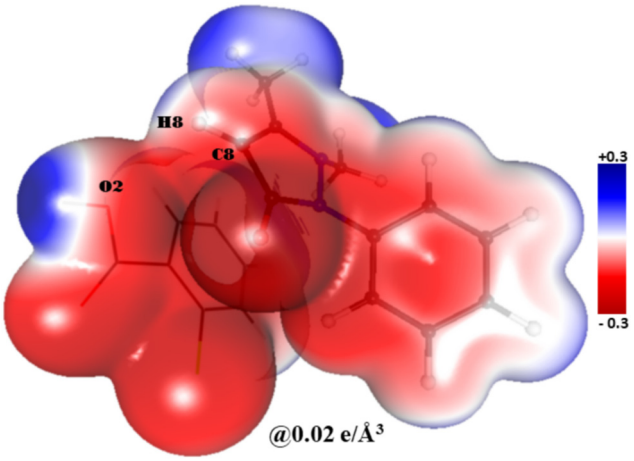

Fig. 7 The 3D electron density surface (contour = 0.02 e $Å^{-3}$) coloured according to electrostatic potential for molecular dimers **AN**···**CBA**^{iii} (iii = $-x + 1, -y + 1, -z + 1$) explains the repulsive behaviour of certain interactions mentioned in Table 4.

face with each other as a consequence of the packing. This may also explain the relatively low thermal stability and relatively weak diffraction at higher angles.

4. Conclusion

Contrary to small molecules, charge density analysis of co-crystals is not very common in the literature mainly due to the fact the co-crystals are usually not well diffracting. In this work, using a knowledge-based approach, we have successfully grown a new co-crystal of an active pharmaceutical ingredient (API), antipyrine with 2-chlorobenzoic acid. Through careful crystallization, we were able to find a crystal that diffracted to reasonably high resolution enabling us to carry out the multipolar refinement. Results from experimental and theoretical charge density analysis are in close agreement, proving the correctness of the refinement strategy and validity of the model. Based on the multipolar model, the packing and stability of the cocrystal have been analysed in terms of electrostatic and topological contributions. We conclude that the driving force behind the formation of the co-crystal is the strong electrostatic attraction between **AN** and **CBA** molecules in the asymmetric unit expressed *via* the formation of a classical O2–H2···O1 hydrogen bond which is characterized by a very short H···A distance, a high value of electron density at the critical point and high values of local energy densities. The total electrostatic interaction energy of this dimer is among the highest values found in the literature. Further, the study of the integrated charges reveals that the pyrazolone ring is very rich in electrons which makes its carbonyl oxygen atom a strong acceptor for hydrogen bonding. This carbonyl carbon is the principal pharmacophoric feature of antipyrine drug. It is argued that cocrystallization begins through this hydrogen bond forming a robust ring synthon. The electrostatic energy values show that the heterodimers between **AN–CBA** are generally more stable than the dimers between pure fragments, **AN–AN**, or **CBA–CBA**. Besides the reference dimer, the crystal structure is largely dominated by weak intermolecular C–H···π, C–H···O, and π···π interaction; especially C10–H10A···C8^{i}, C14–H14···O1^{ii} and C10–H10C···O1^{v} having relatively short bond length, and reasonable values of electron density at critical points. Their electrostatic interaction energies show that most of them are attractive in nature lending stability to the cocrystal assembly, although some of them are repulsive, probably the result of packing. The molecular electrostatic potential surface shows the complementarity between interacting moieties and supports the interaction energy landscape. Since the cocrystal is primarily built upon only a single strong hydrogen bond and since the rest of the interactions are weak, the cocrystal has low thermal stability. This study highlights the significance of using electrostatics to discuss the crystalline solid forms of pharmaceuticals.

Conflicts of interest

There are no conflicts of interest.

Acknowledgements

The authors are grateful to the Higher Education Commission and the Federal Government of Pakistan for funding under the Public Sector Development Programme to establish the

Materials Chemistry Laboratory at The Islamia University of Bahawalpur, Pakistan, which made this study possible.

References

1 W. Guo, S. Du, Y. Lin, B. Lu, C. Yang, J. Wang and Y. Zeng, *New J. Chem.*, 2018, **42**, 15068–15078.
2 L. S. Reddy, S. J. Bethune, J. W. Kampf and N. Rodríguez-Hornedo, *Cryst. Growth Des.*, 2009, **9**, 378–385.
3 D. R. Serrano, P. O'Connell, K. J. Paluch, D. Walsh and A. M. Healy, *J. Pharm. Pharmacol.*, 2016, **68**, 665–677.
4 S. Hiendrawan, B. Veriansyah, E. Widjojokusumo, S. N. Soewandhi, S. Wikarsa and R. R. Tjandrawinata, *Int. J. Pharm.*, 2016, **497**, 106–113.
5 B. Zhu, Q. Zhang, J.-R. Wang and X. Mei, *Cryst. Growth Des.*, 2017, **17**, 1893–1901.
6 S. P. Gopi, M. Banik and G. R. Desiraju, *Cryst. Growth Des.*, 2017, **17**, 308–316.
7 S. Chaudhari, S. A. Nikam, N. Khatri and S. Wakde, *J. Drug Delivery Ther.*, 2018, **8**, 350–358.
8 M. Karimi-Jafari, L. Padrela, G. M. Walker and D. M. Croker, *Cryst. Growth Des.*, 2018, **18**, 6370–6387.
9 N. Blagden, S. Coles and D. Berry, *CrystEngComm*, 2014, **16**, 5753–5761.
10 E. I. Korotkova and B. Kratochvíl, *Procedia Chem.*, 2014, **10**, 473–476.
11 P. Vishweshwar, J. A. McMahon, J. A. Bis and M. J. Zaworotko, *J. Pharm. Sci.*, 2006, **95**, 499–516.
12 S. Kumar, *Indian J. Pharm.*, 2018, **79**, 858–871.
13 G. R. Desiraju, *Angew. Chem., Int. Ed.*, 2007, **46**, 8342–8356.
14 J. Sarma and G. R. Desiraju, *Cryst. Growth Des.*, 2002, **2**, 93–100.
15 P. A. Wood, N. Feeder, M. Furlow, P. T. Galek, C. R. Groom and E. Pidcock, *CrystEngComm*, 2014, **16**, 5839–5848.
16 R. Bader, *Atoms in Molecules: A Quantum Theory*, Oxford University Press, 1990.
17 K. Brune and B. Hinz, *Arthritis Rheum.*, 2004, **50**, 2391–2399.
18 T. Kraemer and H. H. Maurer, in *Handb. Anal. Sep.*, Elsevier, 2008, vol. 6, pp. 319–356.
19 H. A. Merey, *Bull. Fac. Pharm.*, 2016, **54**, 181–189.
20 S. Mahmud and N. Rosen, *Curr. Pain Headache Rep.*, 2019, **23**, 6.
21 Y.-X. Zou, X. Feng, Z.-Y. Chu, W.-H. Liu, X.-D. Zhang and J.-B. Ba, *Regul. Toxicol. Pharmacol.*, 2019, **103**, 34–40.
22 K. M. Elattar and A. A. Fadda, *Synth. Commun.*, 2016, **46**, 1567–1594.
23 A. Bertolini, A. Ottani and M. Sandrini, *Curr. Med. Chem.*, 2002, **9**, 1033–1043.
24 R. Karinen, G. Høiseth, K. O. Svendsen, S. Rogde and V. Vindenes, *Forensic Sci. Int.*, 2015, **248**, e13–e15.
25 M. T. El Sayed, M. A. S. El-Sharief, E. S. Zarie, N. M. Morsy, A. R. Elsheakh, A. Voronkov, V. Berishvili and G. S. Hassan, *Bioorg. Med. Chem. Lett.*, 2018, **28**, 952–957.
26 G. Dannhardt and W. Kiefer, *Eur. J. Med. Chem.*, 2001, **36**, 109–126.
27 T. Singh and M. Vijayan, *Acta Crystallogr., Sect. B: Struct. Crystallogr. Cryst. Chem.*, 1974, **30**, 557–562.
28 D. Yang, R. Wang, G. Jin, B. Zhang, L. Zhang, Y. Lu and G. Du, *Cryst. Growth Des.*, 2019, **19**, 6175–6183.
29 N. Issa, S. A. Barnett, S. Mohamed, D. E. Braun, R. C. Copley, D. A. Tocher and S. L. Price, *CrystEngComm*, 2012, **14**, 2454–2464.
30 S. Alberola, F. Sabon, J. Jaud and J. Galy, *Acta Crystallogr., Sect. B: Struct. Crystallogr. Cryst. Chem.*, 1977, **33**, 3337–3341.
31 K. Lyczko, *Acta Crystallogr., Sect. E: Struct. Rep. Online*, 2013, **69**, o127–o128.
32 S. Alberola, J. Rambaud and F. Sabon, *Ann. Pharm. Fr.*, 1976, **34**(3–4), 95–99.
33 J. Rambaud, B. Jeanjean, B. Pauvert and S. Alberola, *Bull. Soc. Chim. Fr.*, 1986, 620–624.
34 A. Lemmerer, J. Bernstein, U. J. Griesser, V. Kahlenberg, D. M. Többens, S. H. Lapidus, P. W. Stephens and C. Esterhuysen, *Chem. – Eur. J.*, 2011, **17**, 13445–13460.
35 L. K. Mapp, S. J. Coles and S. Aitipamula, *Cryst. Growth Des.*, 2017, **17**, 163–174.
36 M. G. Smith and A. Lemmerer, *J. Mol. Struct.*, 2019, **1175**, 307–313.
37 C. R. Groom, I. J. Bruno, M. P. Lightfoot and S. C. Ward, *Acta Crystallogr., Sect. B: Struct. Sci., Cryst. Eng. Mater.*, 2016, **72**, 171–179.
38 K. Kowalska, D. Trzybiński and A. Sikorski, *CrystEngComm*, 2015, **17**, 7199–7212.
39 S. V. Rao, *Arabian J. Chem.*, 2020, **13**, 6040–6043.
40 S. T. Hassib, G. S. Hassan, A. A. El-Zaher, M. A. Fouad and E. A. Taha, *Spectrochim. Acta, Part A*, 2017, **186**, 59–65.
41 T. Maki and K. Takeda, *Ullmann's encyclopedia of industrial chemistry*, 2000, vol. 3.
42 P. Coppens, *Angew. Chem., Int. Ed.*, 2005, **44**, 6810–6811.
43 J. J. Du, L. Váradi, P. A. Williams, P. W. Groundwater, J. Overgaard, J. A. Platts and D. E. Hibbs, *RSC Adv.*, 2016, **6**, 81578–81590.
44 A. Owczarzak and M. Kubicki, *Crystals*, 2018, **8**, 132.
45 M. Gryl, S. Cenedese and K. Stadnicka, *J. Phys. Chem. C*, 2015, **119**, 590–598.
46 V. R. Hathwar, T. S. Thakur, R. Dubey, M. S. Pavan, T. N. Guru Row and G. R. Desiraju, *J. Phys. Chem. A*, 2011, **115**, 12852–12863.
47 V. R. Hathwar, R. Pal and T. Guru Row, *Cryst. Growth Des.*, 2010, **10**, 3306–3310.
48 T. Nguyen, P. Groundwater, J. Platts and D. Hibbs, *J. Phys. Chem. A*, 2012, **116**, 3420–3427.
49 S. P. Thomas, S. P. K. Veccham, L. J. Farrugia and T. Guru Row, *Cryst. Growth Des.*, 2015, **15**, 2110–2118.
50 P. Munshi and T. N. Guru Row, *Acta Crystallogr., Sect. B: Struct. Sci.*, 2006, **62**, 612–626.
51 T. Steiner, *Crystallogr. Rev.*, 2003, **9**, 177–228.
52 M. U. Faroque, S. Noureen, M. Ahmed and M. N. Tahir, *Acta Crystallogr., Sect. C: Struct. Chem.*, 2018, **74**, 100–107.
53 M. U. Faroque, S. Noureen, S. H. Mirza, M. N. Tahir and M. Ahmed, *Acta Crystallogr., Sect. C: Struct. Chem.*, 2019, **75**, 46–53.

54 A. Iqbal, A. Mehmood, S. Noureen, C. Lecomte and M. Ahmed, *Acta Crystallogr., Sect. B: Struct. Sci., Cryst. Eng. Mater.*, 2021, **77**, 1035–1047.
55 *APEX3, SAINT and SADABS*, Bruker AXS Inc., Madison, Wisconsin, USA, 2016.
56 J. Cosier and A. M. Glazer, *J. Appl. Crystallogr.*, 1986, **19**, 105–107.
57 G. M. Sheldrick, *Acta Crystallogr., Sect. A: Found. Adv.*, 2014, **70**, C1437.
58 I. Usón and G. M. Sheldrick, *Acta Crystallogr., Sect. D: Struct. Biol.*, 2018, **74**, 106–116.
59 F. H. Allen and I. J. Bruno, *Acta Crystallogr., Sect. B: Struct. Sci.*, 2010, **66**, 380–386.
60 C. Jelsch, B. Guillot, A. Lagoutte and C. Lecomte, *J. Appl. Crystallogr.*, 2005, **38**, 38–54.
61 A. Ø. Madsen, *J. Appl. Crystallogr.*, 2006, **39**, 757–758.
62 R. Herbst-Irmer, J. Henn, J. J. Holstein, C. B. Hübschle, B. Dittrich, D. Stern, D. Kratzert and D. Stalke, *J. Phys. Chem. A*, 2013, **117**, 633–641.
63 N. K. Hansen and P. Coppens, *Acta Crystallogr., Sect. A: Cryst. Phys., Diffr., Theor. Gen. Crystallogr.*, 1978, **34**, 909–921.
64 V. R. Hathwar, R. G. Gonnade, P. Munshi, M. M. Bhadbhade and T. N. Guru Row, *Cryst. Growth Des.*, 2011, **11**, 1855–1862.
65 T. H. Nguyen, P. W. Groundwater, J. A. Platts and D. E. Hibbs, *J. Phys. Chem. A*, 2012, **116**, 3420–3427.
66 C. Kalaiarasi, C. George, R. G. Gonnade, V. R. Hathwar and K. Poomani, *Acta Crystallogr., Sect. B: Struct. Sci., Cryst. Eng. Mater.*, 2019, **75**, 942–953.
67 A. Iruthayaraj, K. Chinnasamy, K. K. Jha, P. Munshi, M. S. Pavan and P. Kumaradhas, *J. Mol. Struct.*, 2019, **1180**, 683–697.
68 P. Giannozzi, O. Andreussi, T. Brumme, O. Bunau, M. B. Nardelli, M. Calandra, R. Car, C. Cavazzoni, D. Ceresoli and M. Cococcioni, *J. Phys.: Condens. Matter*, 2017, **29**, 465901.
69 J. P. Perdew, K. Burke and M. Ernzerhof, *Phys. Rev. Lett.*, 1996, **77**, 3865–3868.
70 S. Grimme, J. Antony, S. Ehrlich and H. Krieg, *J. Chem. Phys.*, 2010, **132**, 154104.
71 P. E. Blöchl, *Phys. Rev. B: Condens. Matter Mater. Phys.*, 1994, **50**, 17953–17979.
72 C. F. Macrae, P. R. Edgington, P. McCabe, E. Pidcock, G. P. Shields, R. Taylor, M. Towler and J. van de Streek, *J. Appl. Crystallogr.*, 2006, **39**, 453–457.
73 J. W. Steed, *Trends Pharmacol. Sci.*, 2013, **34**, 185–193.
74 L. Jiang, Y. Huang, Q. Zhang, H. He, Y. Xu and X. Mei, *Cryst. Growth Des.*, 2014, **14**, 4562–4573.
75 B. Guillot, *Acta Crystallogr., Sect. A: Found. Crystallogr.*, 2012, **68**, 204.
76 M. Roumanos and M. Kertesz, *J. Phys. Chem. A*, 2011, **115**, 4832–4839.
77 J. Bernstein, R. E. Davis, L. Shimoni and N. L. Chang, *Angew. Chem., Int. Ed. Engl.*, 1995, **34**, 1555–1573.
78 F. L. Hirshfeld, *Theor. Chim. Acta*, 1977, **44**, 129–138.
79 M. A. Spackman and P. G. Byrom, *Chem. Phys. Lett.*, 1997, **267**, 215–220.
80 J. J. McKinnon, M. A. Spackman and A. S. Mitchell, *Acta Crystallogr., Sect. B: Struct. Sci.*, 2004, **60**, 627–668.
81 M. Turner, J. McKinnon, S. Wolff, D. Grimwood, P. Spackman, D. Jayatilaka and M. Spackman, *CrystalExplorer17*, University of Western Australia, 2017.
82 J. J. McKinnon, D. Jayatilaka and M. A. Spackman, *Chem. Commun.*, 2007, 3814–3816.
83 R. F. Bader, *Acc. Chem. Res.*, 1985, **18**, 9–15.
84 C. Matta and R. Gillespie, *J. Chem. Educ.*, 2002, **79**, 1141.
85 A. I. Stash and V. G. Tsirelson, *J. Appl. Crystallogr.*, 2014, **47**, 2086–2089.
86 S. Swaminathan, B. Craven, M. Spackman and R. Stewart, *Acta Crystallogr., Sect. B: Struct. Sci.*, 1984, **40**, 398–404.
87 M. Spackman, H. Weber and B. M. Craven, *J. Am. Chem. Soc.*, 1988, **110**, 775–782.
88 N. Bouhmaida, N.-E. Ghermani, C. Lecomte and A. Thalal, *Acta Crystallogr., Sect. A: Found. Crystallogr.*, 1997, **53**, 556–563.
89 N. Muzet, B. Guillot, C. Jelsch, E. Howard and C. Lecomte, *Proc. Natl. Acad. Sci. U. S. A.*, 2003, **100**, 8742–8747.
90 A. Volkov and P. Coppens, *J. Comput. Chem.*, 2004, **25**, 921–934.
91 R. Soave, M. Barzaghi and R. Destro, *Chem. – Eur. J.*, 2007, **13**, 6942–6956.
92 B. Fournier, E.-E. Bendeif, B. Guillot, A. Podjarny, C. Lecomte and C. Jelsch, *J. Am. Chem. Soc.*, 2009, **131**, 10929–10941.
93 N. Ghermani, C. Lecomte and Y. Dusausoy, *Phys. Rev. B*, 1996, **53**, 5231–5239.
94 X. Shi, N. El Hassan, A. Ikni, W. Li, N. Guiblin, A. S. De-Biré and N. Ghermani, *CrystEngComm*, 2016, **18**, 3289–3299.
95 Z. Su and P. Coppens, *Acta Crystallogr., Sect. A: Found. Crystallogr.*, 1992, **48**, 188–197.
96 A. Buckingham, *Adv. Chem. Phys.*, 1967, **12**, 107–142.
97 U. Koch and P. L. Popelier, *J. Phys. Chem.*, 1995, **99**, 9747–9754.
98 P. Munshi and T. N. Guru Row, *Crystallogr. Rev.*, 2005, **11**, 199–241.
99 E. Espinosa, I. Alkorta, J. Elguero and E. Molins, *J. Chem. Phys.*, 2002, **117**, 5529–5542.
100 E. Espinosa and E. Molins, *J. Chem. Phys.*, 2000, **113**, 5686–5694.

